



Contents lists available at ScienceDirect

Journal of the Mechanical Behavior of Biomedical Materials

journal homepage: www.elsevier.com/locate/jmbbm

Study of the compression and wear-resistance properties of freeze-cast Ti and Ti–5W alloy foams for biomedical applications



Hyelim Choi^a, Serge Shil'ko^b, Jenő Gubicza^c, Heeman Choe^{a,*}

^a School of Materials Science and Engineering, Kookmin University, 77 Jeongneung-ro, Seongbuk-gu, Seoul 20707, Republic of Korea

^b V.A. Belyi Metal-Polymer Research Institute of National Academy of Sciences of Belarus, 32A Kirov Str., 246050 Gomel, Belarus

^c Department of Materials Physics, Eötvös Loránd University, P.O.B. 32, H-1518 Budapest, Hungary

ARTICLE INFO

Keywords:

Implant
Ti alloy foam
Compressive strain
Wear

ABSTRACT

Ti and Ti–5 wt% W alloy foams were produced by freeze-casting process and their mechanical behaviors were compared. The Ti–5W alloy foam showed a typical acicular Widmanstätten α/β structure with most of the W dissolved in the β phase. An electron-probe microanalysis revealed that approximately 2 wt% W was uniformly dissolved in the Ti matrix of Ti–5W alloy foam with few partially dissolved W particles. The compressive-yield strength of Ti–5W alloy foam (~ 323 MPa) was approximately 20% higher than that of the Ti foam (~ 256 MPa) owing to the solid-solution-strengthening effect of W in the Ti matrix, which also resulted in a dramatic improvement in the wear resistance of Ti–5W alloy foam. The compressive behaviors of the Ti and Ti–5W alloy foams were predicted by analytical models and compared with the experimental values. Compared with the Gibson-Ashby and cellular-lattice-structure-in-square-orientation models of porous materials, the orientation-averaging method provided prediction results that are much more accurate in terms of both the Young's modulus and the yield strength of the Ti and Ti–5W alloy foams.

1. Introduction

Various materials have been used for different implant applications, e.g., polymers for soft biotissues or artificial lenses and strengthened metal alloys or ceramics for load-bearing joints because the required mechanical/physical properties and biocompatibility may vary depending on where and how the implant is used (von Recum, 1999). In particular, metallic implant materials possess superior strength, fracture toughness, ductility, and machinability compared to ceramic implant materials. Nevertheless, they show relatively poor corrosion resistance *in vivo* (Enderle et al., 2005). To overcome this, stainless steels, Ni–Cr alloys, and Ti alloys with a good combination of strength and corrosion resistance have been studied as a replacement candidate for hip/knee joints or dental implants (Oldani et al., 2012; Lina et al., 2008). Among these materials, Ti and Ti-based alloys are considered attractive because of their excellent corrosion resistance as well as several other outstanding properties. First, a dense, thin TiO₂ film forms easily on the surface of Ti, giving rise to the superior corrosion resistance (Donachie, 2004). Second, the formation of TiO₂ on the surfaces of Ti alloys takes place quickly, which is approximately 55% and 330% faster than the formation of oxide films on the surfaces of Co–28Cr–6Mo and 316L stainless steel (Geetha et al., 2009). Third, the

formation of direct bonding is feasible between the Ti or Ti alloy and osseous tissue (Adell et al., 1970), and this bonding is strong and tough because it forms stable, biocompatible, and non-toxic CaTiO₃ by combining TiO₂ and Ca ions from the hydroxyapatite in the osseous tissue (Liu et al., 2004).

Unfortunately, Ti does not possess sufficient strength or wear resistance for use as bone substitute material in high load-bearing applications, e.g., femoral heads for hip replacement. Efforts have been made to achieve the required mechanical properties through hardened Ti alloys or Ti composites reinforced with hard ceramic particles (Iijima et al., 2003). Despite some improvements in strength, efforts are still being made toward further improvements including reduction of the elastic modulus of bulk Ti alloys or composites with significantly higher moduli than natural human bone; however, the issue of the stress-shielding effect still remains. The moduli of bulk Ti-based bone substitute material and its alloys (55–117 GPa) (Geetha et al., 2009; Li et al., 2004; Krishna et al., 2007) must further reduced down to be in closer agreement with that of natural bone (~ 40 GPa (Wang et al., 2013)) to minimize the stress-shielding effects. Indeed, the presence of the stress-shielding effect can cause a serious setback; it prevents the external load from being adequately transferred to the bone and is thus supported primarily by the implant material, which can eventually

* Corresponding author.

E-mail address: heeman@kookmin.ac.kr (H. Choe).

<http://dx.doi.org/10.1016/j.jmbbm.2017.04.020>

Received 21 January 2017; Received in revised form 23 March 2017; Accepted 17 April 2017

Available online 21 April 2017

1751-6161/ © 2017 Elsevier Ltd. All rights reserved.

cause degradation and fracture, or osteoporosis in the bone (Choi et al., 2014).

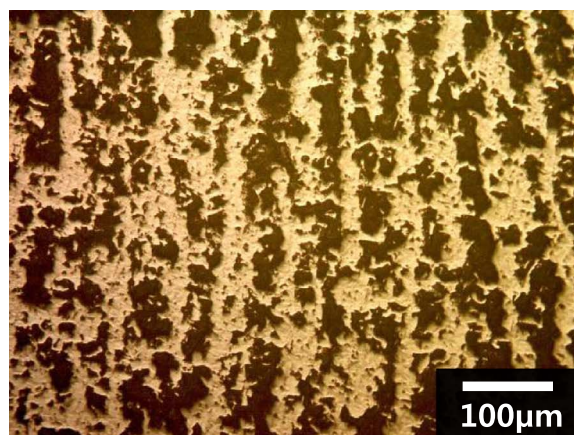
We thus investigate Ti and Ti alloy foams synthesized by freeze-casting. In particular, there has been an increasing recent interest in freeze-casting of porous metals (Li and Dunand, 2011; Jo et al., 2016; Park et al., 2017), because the processing method generally forms a directional, elongated pore structure that is advantageous for biomedical or implant applications (Deville, 2010). To precisely control pore size, morphology, and porosity, a good understanding of the solidification behavior of the powder slurry is important. This study reports the microstructure and compressive and wear behaviors of Ti–5W alloy foams for their potential use in implant applications. For compressive behavior, we compare the results between Ti and Ti–5W foams using both experimental data and model predictions.

2. Material and methods

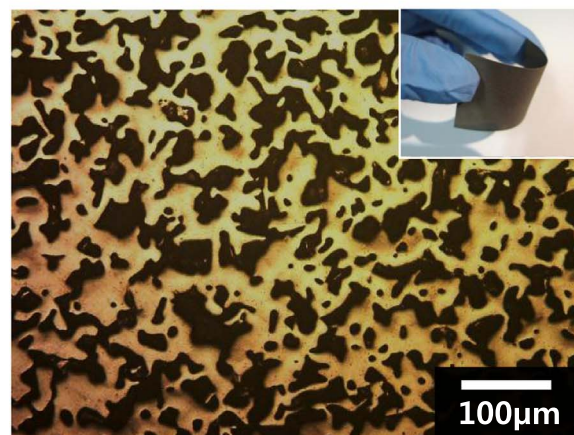
The Ti powder (Alfa Aesar, MA, USA) consisted of ~ 325 mesh-sized particles, whereas W powder (Atlantic Equipment Engineers, NJ, USA) consisted of $1\text{-}\mu\text{m}$ particles for all experiments. First, 0.28 g of poly (vinyl alcohol) (PVA, Mw 89,000–98,000, purity $\sim 99\%$, Sigma-Aldrich Co., MO, USA) was dissolved in 10 ml of distilled water, and 10.69 g of Ti powder and 0.56 g of W powder were added to the prepared solution to complete the slurry. The slurry was then poured directly on top of the Cu chiller block standing in a stainless-steel vessel under cooled by liquid N_2 . To ensure thermal protection along the horizontal direction and promote heat transfer through contact between the slurry and the Cu rod, the slurry was carefully wrapped by polystyrene foil that had been inserted into a polymer mold. The Cu chiller rod was 60 mm in diameter and the freezing rate was $-10\text{ }^\circ\text{C}/\text{min}$. The frozen green-body was lyophilized in a freeze-dryer (OPR-FDU-7003, Operon, Republic of Korea) to remove ice through sublimation at $-90\text{ }^\circ\text{C}$ and 0.67 Pa for ~ 24 h. The lyophilized green-body was then sintered in a vacuum furnace via a two-step heat-treatment process: at $300\text{ }^\circ\text{C}$ for 3 h and then at $1050\text{ }^\circ\text{C}$ for 6 h. The final Ti and Ti-W foam were 4 cm in diameter and 2 cm in thickness. These samples were machined for mechanical tests. The elastic modulus was obtained by measuring the slope of the linear region of stress-strain curve from the compression test.

The Microhardness was measured using a Vickers hardness tester (Miyutoyo, Tsukuba, Japan) with an applied load of 30 g and a dwell time of ~ 10 s. The microstructure was examined using both optical and scanning electron microscopy (SEM, JEOL JSM-7610F, Japan), along with an electron-probe micro-analyzer (EPMA, JEOL JXA-8500F, Japan) after being etched with Kroll's reagent (6 ml nitric acid, 2 ml HF, and 92 ml water). The degrees of continuity (C_s) of the Ti and Ti–5W foam struts were metallographically assessed based on the microstructural SEM images by measuring the contiguity parameters N^{SS} and N^{SP} , (where, N^{SS} and N^{SP} are the numbers of intercepts of the strut/strut and strut/pore interfaces, respectively) which were determined using simple intercept measurements by drawing more than ten random unit lines on the polished specimen surfaces.

Some samples were cut into parallelepiped specimens with dimensions of $3\text{ mm} \times 3\text{ mm} \times 6\text{ mm}$ for the room-temperature compressive test (Z020, Zwick, Germany). Uniaxial compression tests were carried out at room temperature at a nominal strain rate of 0.001 s^{-1} . The wear tests were performed using a ball-on-disk tribometer tester (RB 102 PD, R & B, Republic of Korea). Disk specimens with diameters of 23 mm were loaded and slid against an abrasive Al_2O_3 counterpart ball (Samhwa Ceramics, Republic of Korea; purity: 93%; Mohs hardness number: 9) at a sliding speed of 0.1 m/s. The applied normal load was fixed at 20 N and the total sliding distance traveled by the ball ranged from 0 to 2000 m.



(a)



(b)

Fig. 1. Optical images of freeze-cast Ti foams showing that the microstructure of the Ti foam can change from (a) a directional, lamellar pore structure to (b) an irregular, random pore structure with increasing freezing rate. Inset in (b) demonstrates decent flexibility of the Ti foam with random smaller pores.

3. Results

3.1. Microstructure and pore morphology

The microstructure was examined using both optical microscopy (Fig. 1) and SEM (Fig. 2). Fig. 1 compares two different microstructures of Ti foams frozen at fast and slow velocities to demonstrate that it is possible to achieve different pore morphologies via freeze-casting. In the optical images of Fig. 1, the brighter portion represents the Ti struts and the darker portion represents pores. In the radial section (cut along the freezing direction) of Fig. 1(a), Ti foam shows elongated pores distributed regularly (porosity = 55%), as obtained by freezing the suspension at a relatively high mold-bottom temperature of $-10\text{ }^\circ\text{C}$; more specifically, colonies of aligned, lamellar pores are seen replicating those of ice dendrite. The speed of directional growth during freezing is $\sim 100\text{--}1000$ -fold higher in the parallel direction, rather than the perpendicular direction, to the temperature gradient (Li and Dunand, 2011). On the other hand, in Fig. 1(b), Ti foam has randomly distributed smaller pores (porosity = 56%), obtained with more rapid cooling (i.e., by freezing the green body at a relatively low mold-bottom temperature of $-40\text{ }^\circ\text{C}$). The sample frozen at $-10\text{ }^\circ\text{C}$ exhibits a lamellar pore structure typically found in normal ice crystals. Through a moderate temperature gradient (driving force) and sufficient time to create long ice dendrites, the freezing process normally develops pores aligned perpendicularly to the mold-bottom surface. On the other hand, some degree of gradient in powder density exists along the freezing

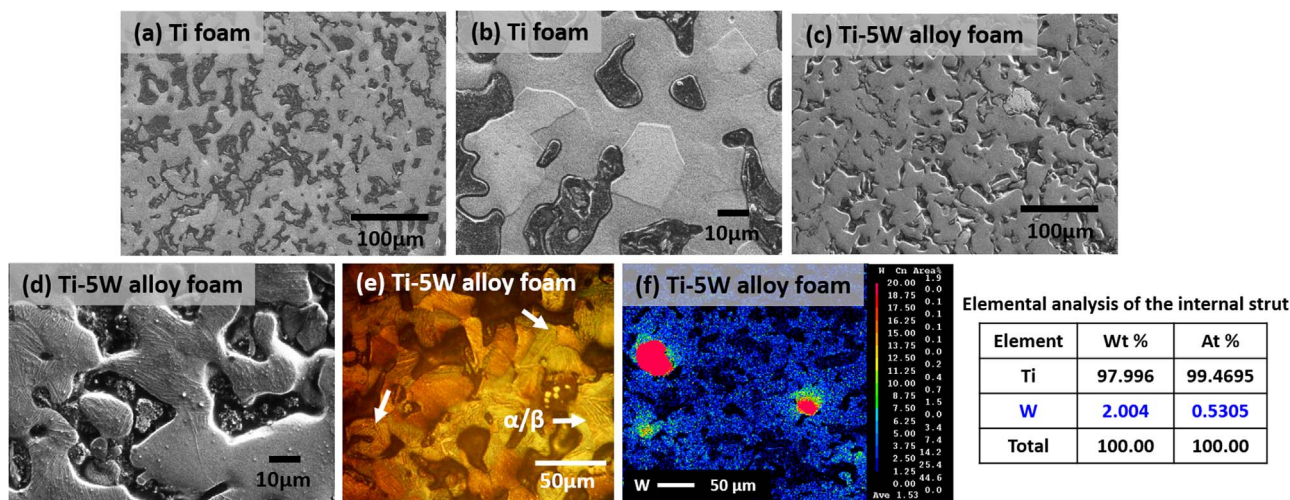


Fig. 2. SEM images of (a-b) Ti and (c-d) Ti–5W alloy foams after being etched with Kroll's reagent; (e) optical image of Ti–5W alloy foam which included α/β widmanstätten structure (f) EPMA analysis on the polished surface of the Ti–5W alloy foam showing the uniform dissolution of W in the Ti matrix also containing a few partially undissolved Ti particles.

direction due to the relatively slow freezing speed (Li and Dunand, 2011); i.e., more powders are piled up near the bottom with a less clear directionality and fewer powders are available at the top with more clear directionality. The sample frozen at $-40\text{ }^\circ\text{C}$ exhibits equiaxed random ice crystals that later form small spherical pores distributed randomly inside the foam owing to the relatively rapid cooling rate. Microstructural observation through both SEM and optical microscopy confirms that the three-dimensional Ti struts are well connected in both cases, with the pores being distributed uniformly.

The degree of strut continuity was estimated and compared by measuring the contiguity, C_s , for the two Ti foams with different morphologies (elongated vs. equiaxed) following Fan's approach in Refs. Gurland (1958) and Fan et al. (1993):

$$C_s \approx \frac{2N^{SP}}{2N^{SS} + N^{SP}} \quad (1)$$

where N^{SS} and N^{SP} are the numbers of intercepts of the strut/strut and strut/pore interfaces, respectively, within more than ten random lines of unit length on the examined fracture surfaces. The degree of contiguity was considerably different between the two microstructures. The strut structure in the Ti foam with equiaxed pore structure appears to be better connected and more continuous ($C_s=0.49$, Fig. 1(b)) than that in the Ti foam with longitudinal pore structure ($C_s=0.29$, Fig. 1(a)), suggesting that faster freezing by the lower mold-bottom temperature could be more beneficial for improving the ductility and flexibility of the Ti foam by increasing the continuity of the structure of the Ti struts shown in the inset of Fig. 1(b). This is emphasized particularly because, in most cases, the mechanical integrity (e.g., flexibility) of metal foams is insufficient to support load-bearing applications or even for functional applications when used in the form of thin film.

Fig. 2(a)–(d) shows SEM micrographs of the cross-sections of Ti (a-b) and Ti–5W (c-d) alloy foams fabricated by freeze-casting, along with an EPMA image of the dissolution of W in Ti–5W alloy foam; here, both foams exhibit random pore structure as a result of rapid cooling. After being etched with Kroll's reagent (6 ml nitric acid, 2 ml HF, and 92 ml water), individual grains are clearly observed on the struts of the Ti foam (Fig. 2(b)). When alloyed with W, the etched Ti–5W foam shows an acicular Widmanstätten α/β structure with most of the W dissolved in the β phase (Donachie, 2004; Frary et al., 2003; Choe et al., 2005). On the other hand, EPMA analysis revealed that W dissolution in the Ti–5W alloy foam is ~ 2 wt% with some partially dissolved W particles remaining as shown in Fig. 2(e–f). The black-colored areas represent pores, the lighter areas represent the struts of Ti–5W alloy foam, and

the white-colored rough areas represent the region where W particles are partially dissolved. The presence of the partially dissolved W particles is due to the sample having been fabricated in a solid-state process using the relatively shorter sintering time and lower temperature than those required for the liquid-state diffusion process. It is thought that W dissolution would have been almost complete in the Ti–5W alloy foam if a sufficiently high sintering temperature and time were to be used, given the relatively small W average powder sizes ($\sim 1\text{ }\mu\text{m}$) (Frary et al., 2003; Choe et al., 2005). However, the pore size and structure could have been affected if higher sintering temperature and longer time were used, eventually leaving a reduced number of pores and pore volume. According to the mapping analysis by EPMA for the location and dispersion of W, there are only a few undissolved W particles observed and the rest of the W particles are evenly dissolved and distributed in the Ti matrix. The typical Widmanstätten α/β structure is also observed in the Ti–5W alloy foam strut.

3.2. Hardness and compressive strength

Vickers-hardness measurements were performed on both Ti and Ti–5W alloy foam samples to examine their hardness; in particular, the effect of W dissolution on the hardness of Ti foam was investigated (Table 1). The difference in the Vickers hardness values is relatively large between the Ti foam (2265 ± 187 HV (MPa)) and Ti–5W alloy foam (2658 ± 372 HV(MPa)) in good agreement with previous studies (Donachie, 2004; Mante et al., 1999). In other words, the Vickers hardness of the Ti–5W alloy foam is approximately 17% higher than that of the Ti foam. The considerably higher Vickers hardness value of the Ti–5W alloy foam as compared to that of the Ti foam suggests that the dissolution of W in the Ti foam matrix and its subsequent strengthening of the solid solution is highly effective. This result that is in good agreement with the observation from Fig. 2(f) showing the apparent dissolution of W in the Ti matrix (Choe et al., 2005, 2008).

Fig. 3 compares the compressive behavior at ambient temperature for the Ti and Ti–5W alloy foams. The samples tended to follow the

Table 1
Vickers hardness values of Ti and Ti–5W alloy foams evaluated in this study.

	Before wear	After wear
Ti foam (porosity 32%)	2265 ± 187 HV (MPa)	5090 ± 422 HV (MPa)
Ti–5W alloy foam (porosity 39%)	2658 ± 372 HV (MPa)	5580 ± 432 HV (MPa)

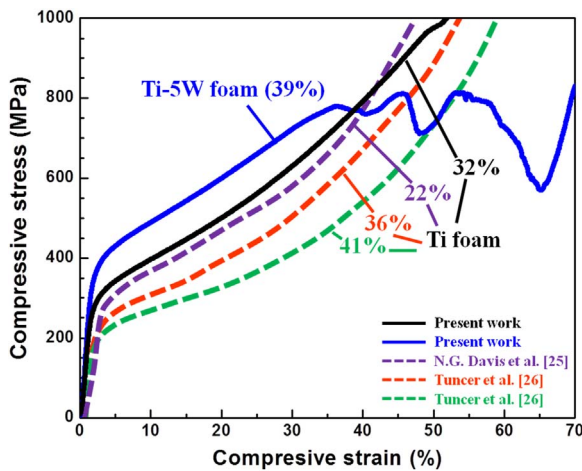


Fig. 3. Compressive stress–strain curves of Ti and Ti–5W alloy foams with 32 and 39% porosity, respectively, in comparison with those of other Ti foams reported in previous literature (Davis et al., 2001; Tuncer and Arslan, 2009).

Table 2

Young's modulus and yield-strength values of Ti and Ti–5W alloy foams are compared with the analytically calculated values (orientation-averaging method) and those predicted by the Gibson–Ashby (G-A) and cellular-lattice-structure-in-square-orientation (C-L) models. The numbers in parentheses are error percentage.

Ti foam (porosity 32%)	Young's modulus (GPa)	Yield strength (MPa)	Ti–5W foam (porosity 39%)	Young's modulus (GPa)	Yield strength (MPa)
Experimental value	19.8	256.2	Experimental value	25.4	322.6
Present prediction (orientation averaging)	29.3 (32%)	220.8 (–16%)	Present prediction (orientation averaging)	23.0 (–10%)	289.5 (–11%)
G-A model	55 (64%)	123.6 (–107%)	G-A model	53.8 (53%)	182.1 (–77%)
C-L model	40.8 (52%)	249.9 (–3%)	C-L model	39.0 (35%)	365.4 (12%)

typical ductile metallic behavior with linear elasticity at low stresses, a collapse plateau, and finally a densification regime in which stress rises steeply (Jorgensen and Dunand, 2011). Both samples show elastic behavior up to a strain of 2–3%, followed by a long plastic-deformation behavior. Strain-hardening behavior is seen for both the Ti and Ti–5W alloy foams in the plastic region up to ~60%, where the stress dramatically decreased in the Ti–5W alloy foam. Even with the presence of some cracks and fractures inside the foam, the three-dimensionally connected struts in the foams could probably withstand high stresses and finally have high compressive strengths up to near-complete deformation. Despite its higher porosity (39%), the Ti–5W alloy foam exhibits a yield strength of 323 MPa, which is ~20% higher than that of the Ti foam (256 MPa) with 32% porosity; this is again attributed to the efficient solid-solution-strengthening effect of W in the Ti matrix (Table 2).

Fig. 3 also shows the compressive stress–strain curves for Ti and Ti–5W alloy foams with 32 and 39% porosity, respectively, in comparison with other Ti foams with similar porosities in the literature (Davis et al., 2001; Tuncer and Arslan, 2009). While the compressive strengths of porous metals decrease with increasing porosity, it is of interest to note that our Ti foam with 32% porosity indeed shows 15% higher strength than the Ti foam with 22% porosity produced by Davis et al. (2001). It is also remarkable that our Ti foam with open pore structure shows higher compressive strength than Tuncer's Ti foam with

a similar porosity and closed pore structure (usually with higher mechanical integrity). As shown in Fig. 3, our Ti foam with 32% porosity shows significantly higher strength than the Ti foam with a similar range of porosity of 36% produced by Tuncer and Arslan (2009). This superior compressive strength of our Ti foam is attributed to the difference in morphology. In other words, our Ti foam has randomly distributed finer pores (on the order of a few tens of micrometers) achieved by a combination of powder-metallurgy and freeze-casting method. On the other hand, the Davis's and Tuncer's Ti foams have pores that are coarser by approximately an order of magnitude (on the order of a few hundred micrometers); they are produced by a space-holder method using macro-sized carbamide (CO (NH₂)₂) and a hot-isostatic pressing method using Ar gas, respectively (Hong et al., 2011). Ti and Ti–5W alloy show the compressive behavior of the metal foam in general (Li and Dunand, 2011). Unlike the typical brittle ceramic foams, both Ti and Ti–5W alloy foams show no sign of brittleness in the regime of the collapse plateau. While ceramic foams generally show brittle serrated regions in the stress-strain curve, our Ti–5W alloy foam is strong but does not exhibit ceramic-like serrated brittle behavior. Despite some degree of serrations observed in Ti–5W alloy foam, the struts appear to be rather maintained until densification, perhaps because the dissolution of W in the Ti matrix may not be completely uniform in the entire sample thus resulting in occasional serrated plastic collapse regions, although it significantly strengthens the overall plastic deformation behavior of the Ti–5W alloy foam. In particular, the strengthened Ti–5W alloy foam did not spall or split up until the maximum strain measured.

Several analytical models have been proposed to theoretically describe and predict the compressive behavior of metallic foams. The yield stress of open-cell metallic foams has been described based on the formation of plastic hinges at the strut joints (Gibson and Ashby, 1982). The predictions made by the Gibson–Ashby (G-A) (Eqs. (2) and (3)) and cellular-lattice-structure-in-square-orientation (C-L) models (Eqs. (4) and (5)) are evaluated and compared with the experimental values of the yield strength and Young's modulus for the Ti and Ti–5W alloy foams. First, the Young's modulus of the G-A model is presented as follows:

$$\frac{E^*}{E_s} = C_1 \left(\frac{\rho}{\rho_s}\right)^2 \tag{2}$$

where C_1 is a constant equal to unity, and E_s and ρ_s are the Young's modulus and the density of the corresponding bulk material, respectively. $E_s = 120$ GPa and $\rho_s = 4.51$ g cm^{–3} were taken for pure Ti (Mante et al., 1999). Second, the yield strength of the G-A model is also presented as follows:

$$\frac{\sigma^*}{\sigma_s} = C_2 \left(\frac{\rho}{\rho_s}\right)^{\frac{3}{2}} \tag{3}$$

where C_2 is a constant equal to 0.3 and σ_s is the yield strength of the corresponding bulk material. On the other hand, the Young's modulus and yield strength of the cellular-lattice-structure-in-square-orientation (C-L) model are presented as follows (Hong et al., 2011):

$$\frac{E^*}{E_s} = C_3 \left(\frac{\rho}{\rho_s}\right) \tag{4}$$

$$\frac{\sigma^*}{\sigma_s} = C_3 \left(\frac{\rho}{\rho_s}\right) \tag{5}$$

Here, $C_3 = 0.5$ is based upon the volumetric ratio of the vertical to total struts.

A value of 735 MPa was taken for σ_s , which corresponds to the reported yield strength of pure Ti with the common oxygen (O) content of 0.55 wt% (Mante et al., 1999; Hong et al., 2011). This highly estimated yield strength is most likely attributed to the strengthening effect of O inclusion in Ti. In fact, some O inclusion in Ti during the

freeze-casting process is inevitable. Therefore, the yield strength of 735 MPa for Ti with O inclusion is estimated on the basis that the mean O content included in Ti is approximately 0.5 wt% in Ti foam when processed with a slurry-based method (Mante et al., 1999; Hong et al., 2011).

Based on the same analogy, the σ_s of bulk Ti–5W is estimated to be 1059 MPa (Frury et al., 2003), because the yield strength of 1059 MPa corresponds to that of Ti–5W alloy with ~ 0.5 wt% O, which is increased by 78% from the reported yield-strength value of 595 MPa for Ti–5W alloy (Erk et al., 2008). Additionally, values of $E_S = 113$ GPa, and $\rho_S = 5.25$ g cm $^{-3}$ were also taken for Ti–5W alloy (Erk et al., 2008). It is also anticipated that both the Ti and Ti–5W alloy foams will contain a small percentage of carbon (C), which originates from the PVA binder used for slurry preparation. However, this study considers only the effect of O inclusion, which is reported to have a much more dramatic effect upon the mechanical properties of Ti than does C inclusion (Mante et al., 1999).

As displayed in Table 2, Ti and Ti–5W alloy foams show experimental yield strengths of 256.2 MPa and 322.6 MPa, respectively, which are greater than those predicted by the G–A model (123.6 MPa and 182.1 MPa, respectively). This is most likely because the G–A model is based on the assumption of a weakly-structured metallic foam experiencing plastic bending deformation (Fig. 4(b)), whereas the Ti and Ti–5W alloy foams fabricated in this study have a porous structure whose struts are random and more strongly connected in 3-D (Fig. 4(a)). On the other hand, the C–L model exhibits closer yield strengths of 250 MPa and 365 MPa for Ti and Ti–5W alloy foams, respectively, as compared to the experimental yield strength values. This may be because our Ti foams have porous structures, with fine pores regularly distributed on the order of a few tens of micrometers, and the C–L model in the well-defined square orientation seems more suitable for the description of our Ti foams (Fig. 4(c)) (Mante et al., 1999; Moongkhaklang et al., 2008; Queheillalt et al., 2007).

Table 2 also displays the experimental Young's moduli of 19.8 GPa and 25.4 GPa for Ti and Ti–5W alloy foams, respectively, being much less than those predicted by the G–A (55.0 MPa and 53.8 MPa) and C–L (40.8 MPa and 39.0 MPa) models. One possible reason for this discrepancy is local microplasticity at low-strain levels in compression testing, resulting in near-linear stress–strain slopes that are lower than the actual Young's modulus values. One can indeed measure the Young's modulus of porous materials using an ultrasonic measurement with better accuracy (Choe et al., 2008; Gibson and Ashby, 1997; Thelen et al., 2004).

3.3. Wear resistance

We evaluated and compared the wear resistances of the Ti and Ti–5W foams via pin-on-disk-wear testing. Fig. 5(a)–(b) shows the wear-loss curves for the Ti bulk and Ti foam samples with various sliding distances. The wear mass loss is represented in the unit of lost sample mass (g) (Fig. 5(a)) experimentally measured at selected sliding distances, as well as in the lost sample masses normalized or by the sample's density (g/ ρ) (Fig. 5(b)). Fig. 5(a) shows that the wear loss increased considerably faster for the Ti bulk sample than for the Ti foam sample over the sliding distance of 300–2000 m. However, the discrepancy between the wear mass losses of the Ti bulk and Ti foam samples is much smaller when they are normalized by their densities, which is also true for the wear mass losses of the Ti–10W bulk and Ti–5W foam samples (Fig. 5(b)); here, it is noted that the wear mass loss of the Ti–5W foam is compared with that of the Ti–10 W bulk in Fig. 5(b) due to the unavailability of Ti–5W bulk wear data. It is however seen from the comparison that the addition of W in Ti certainly influences the wear properties of Ti. In particular, the Ti–5W foam sample shows less wear mass loss than the Ti foam sample up to a sliding distance of 2000 m, despite the very similar wear behaviors of the near-linear relationships between wear mass loss and

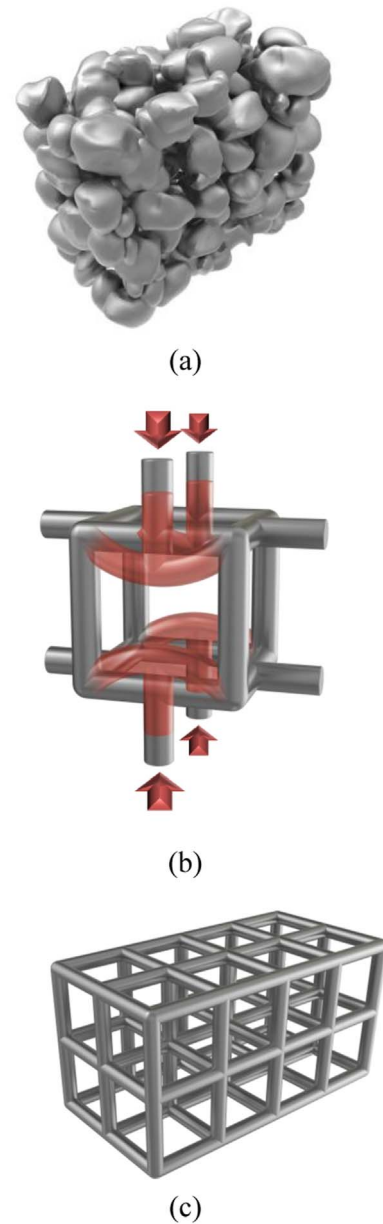


Fig. 4. Schematics of (a) Ti foam structure (present work) with random, 3-D connected pores, (b) the unit cell assumed in the Gibson and Ashby model, and (c) the cellular lattice structure in square-orientation model.

sliding distance.

In Fig. 5(c), the wear rate is shown against the sliding distance for the Ti and Ti–5W foam samples. Up to 200 m, the wear rates of both the samples sharply decreased, with the Ti foam showing approximately four times higher wear rate than the Ti–5W foam sample in this regime (Fig. 5(c)). Moreover, the wear rate of the Ti–5W foam sample continues to be lower than that of the Ti foam sample up to a sliding distance of 2000 m, in spite of the decreasing difference between their wear rates. This observation of the greater wear resistance of the Ti–5W alloy foam is in good agreement with the general trend found in other metallic alloys in which the wear resistance of an alloy is superior to that of its pure metallic counterpart (Dearnley et al., 2004; Venkataraman and Sundararajan, 2000).

During the wear test, wear debris and surface oxides were observed on both samples, as confirmed by EDX results on the tested samples (data not presented in this study). We also compared the surface-hardness values before and after the wear test. After a wear distance of 2000 m, Ti foam sample exhibited a hardness value that was roughly

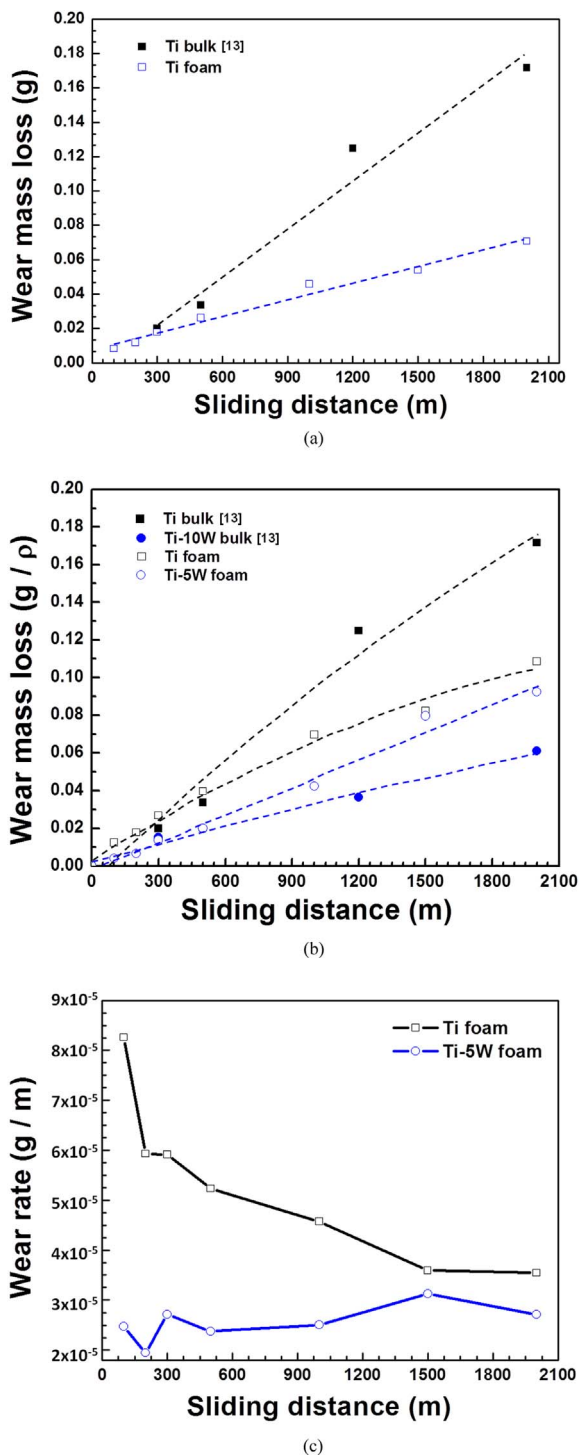


Fig. 5. Comparison of (a) the wear mass losses of the Ti bulk and foam samples, (b) the wear mass losses normalized by the density of the Ti bulk, Ti foam, Ti–5W alloy foam, and Ti–10W bulk samples, and (c) the wear rates of Ti foam and Ti–5W alloy foam as functions of sliding distance.

two times higher (5090 ± 422 HV(MPa)) than the initial hardness (2265 ± 187 HV (MPa)) (Table 1). Similarly, Ti–5W alloy foam exhibited a dramatically increased hardness value after a wear distance of 2000 m (5580 ± 432 HV (MPa)), maintaining a roughly 10%-higher value than that of the Ti foam until the end of the test. The hardness is generally known to be linearly proportional to the wear resistance (Jiang et al., 2000), and our experimental results appear to follow this relationship.

Fig. 6 shows SEM images of (a) Ti foam and (b) Ti–5W alloy foam

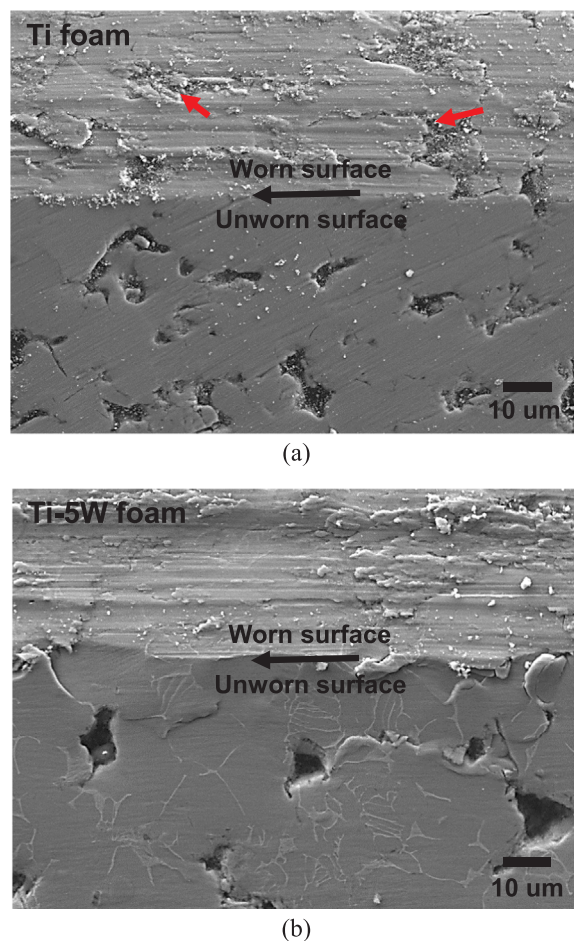


Fig. 6. SEM images of worn surfaces shown in the upper part (in comparison with unworn surfaces shown in the lower part) of (a) Ti foam and (b) Ti–5W alloy foam after the wear test at a sliding speed of 0.1 m/s and a traveled distance of 2000 m under a load of 20 N. Arrows indicate crater marks and compressed wear debris observed on the softer Ti foam.

samples after the wear test. For clearer comparison, the lower part of the image shows a region not subjected to the wear test, whereas the upper part shows a region that was subjected to it and shows the distinct wear grooves as a result. Comparing the worn regions (upper parts) between the two samples, the relatively softer Ti foam sample tends to exhibit crater marks caused by the weighted sliding ball (indicated by arrows); compressed wear debris from the craters (cenospheres) were indeed observed on its surface (Mondal et al., 2009). On the other hand, the relatively stronger Ti–5W alloy foam tends to exhibit a relatively smoother compressed wear surface with closed pores without any evidence of craters or cracking; this is attributed to the solid-solution strengthening effect caused by W addition, in good agreement with the improved hardness and less wear loss.

4. Discussion

4.1. Analytical prediction of the Young's moduli and yield strengths of Ti and Ti–5W alloy foams

A new analytical technique for predicting the mechanical properties of porous materials was earlier suggested by Shi'ko and coworkers (Shi'ko, 2011; Goldade et al., 2016). This was based on an orientation averaging over the deformation energy of the unit rod (tension bar), and thus this analytical technique is hereafter called the “orientation-averaging method”. Within the framework of this method, one can obtain analytical expressions for the effective Young modulus, E^* , and the Poisson's ratio, ν^* , of the considered porous material as follows:

$$\nu^* = \frac{\epsilon_n}{\epsilon_l} = \frac{4 - qk}{16 + qk} \tag{6}$$

$$E^* = \frac{\sigma_l}{\epsilon_l} = E_s \frac{Nq}{10\pi} [1.5 - \nu^* + 0.25q(1 + \nu^*)k] \tag{7}$$

Here, the parameters q and k are introduced for simplicity:

$$q = \frac{S}{L^2} = \frac{4\pi\rho^*}{3N}, \quad k = \left(\frac{L}{L_b}\right)^3 = \frac{3\sqrt{3}}{(\sqrt{3} - \sqrt{\rho^*})^3} \tag{8}$$

In these expressions, σ_l is the axial stress in the uniaxial-stress state of the porous material; ϵ_l and ϵ_n are the corresponding longitudinal and transverse strains of the porous material; L and L_b are respectively the overall length of the rod and the length over which the bending process occurs; S is the cross-sectional area of the rod; E_s is the Young modulus of the solid phase; and N is the number of the rods connected in joint. The parameter ρ^* is characterized by the relative density of the porous material and determined by the ratio as follows:

$$\rho^* = \frac{\rho}{\rho_s} = 1 - \Pi. \tag{9}$$

Here, ρ and ρ_s are the densities of the porous material and the corresponding solid material, respectively; Π is the porosity of the porous material.

Two separate processes should be considered for the calculation of the yield strength, σ_y^* , of the porous material at compression. If the material fracture is caused by the stability loss of the vertically oriented tension bars, then the yield strength is determined by the ratio

$$\sigma_y^* = E_s \frac{q^2\pi}{48} \tag{10}$$

If the plasticity zones arise until the stability loss of the tension bars, then the yield strength should be calculated by the formula

$$\sigma_y^* = \sigma_s \frac{q}{\pi} \tag{11}$$

Here, σ_s is the yield strength of the corresponding solid material. The yield strength of the porous material at compression equals the lesser value determined by Eqs. (10) and (11). However, the estimated yield strengths based on Eqs. (10) and (11) tend to be lower than their actual experimental values. We thus consider only the rods oriented along the loading direction when we derive these relations. In this case, the relation of the normal force and the axial macroscopic stress in a bar has the form: $F_l = \sigma\pi L^2 \cos\theta$.

Here, θ is the angle between the bar and the loading direction. The given expression for normal force in the bar should be averaged over part of the surface of a unit sphere (Supplementary Fig. S1), which is then expressed for a bar as

$$\langle F_l \rangle = \frac{N}{4\pi} \int_0^\alpha \int_0^{2\pi} \sigma\pi L^2 \cos\theta \sin\theta \, d\varphi d\theta = \sigma\pi L^2 \frac{N}{4} (1 - \cos^2\alpha)$$

Additionally, the value of angle α is determined by the normalization condition

$$1 = \frac{N}{4\pi} \int_0^\alpha \int_0^{2\pi} \sin\theta \, d\varphi d\theta = \frac{N}{2} (1 - \cos\alpha) \Rightarrow \alpha = \arccos(1 - \frac{2}{N})$$

Therefore,

$$\langle F_l \rangle = \sigma\pi L^2 (1 - \frac{1}{N})$$

The expression for the yield strength of the considered porous materials can thus be written with account for the above refinement as

$$\sigma_y^* = \min\{E_s \frac{q^2\pi N}{48(N-1)}, \sigma_s \frac{qN}{\pi(N-1)}\} \tag{12}$$

Taking the previously given values of $E_s = 120$ GPa, $\sigma_s = 735$ MPa, and $\rho_s = 4.51$ g cm⁻³ for Ti foam with porosity $\Pi = 0.324$, and the values of $E_s = 113$ GPa, $\sigma_s = 1059$ MPa, and $\rho_s = 5.25$ g cm⁻³ for Ti–5W alloy foam with porosity $\Pi = 0.385$, the calculated values of Young's modulus and yield strength are 29.3 GPa and 220.8 MPa for Ti alloy foam and 23.0 GPa and 289.5 MPa for Ti–5W alloy foam, respectively (Table 2). Here, using the developed calculation technique outlined by Eqs. (6)–(9) and (12), we set $N = 4$. The experimental data and calculation results derived by the orientation-averaging method are presented and compared, along with the prediction values from G-A and C-L models in Table 2. The relative differences between the calculated and experimentally obtained values are also displayed in percent form in brackets in Table 2. It is noted that the orientation-averaging method provides considerably more accurate prediction results than those from the G-A and C-L models for both the values of Young's modulus and the yield strength of the Ti and Ti–5W alloy foams.

The better prediction accuracy of the orientation-averaging method over both the G-A and C-L models is attributed to two factors. First, the G-A and C-L models are both limited to metal foams with relatively high porosities of more than ~70%, whereas the orientation-averaging model covers a greater range of porosity with reasonable accuracy and is thus also suitable for metal foams with lower porosity. Second, some degree of prediction error also originates from the fact that the models do not take into account of the influence of nodes and only consider rod bending, whereas the present orientation-averaging method considers both nodes and bending for the analytical calculation.

5. Conclusions

Ti and Ti–5W alloy foams were produced by freeze-casting and compared. The microstructures of both foams were observed after etching. Ti–5W alloy foam showed an acicular Widmanstätten α/β structure with most of the W segregated into the β phase, in agreement with the previous literature. EPMA analysis revealed that approximately 2 wt% W was dissolved in the Ti–5W alloy foam, with some partially dissolved W particles visibly observed. In particular, the compressive yield strength of the Ti–5W alloy foam (323 MPa) is approximately 20% higher than that of the Ti foam (256 MPa), due to the solid-solution strengthening effect of W in the Ti matrix. The experimental results were also compared with the results predicted from theoretical models. Compared with the G-A and C-L prediction models, the orientation-averaging method provides prediction results that are much more accurate in terms of both the Young's modulus and the yield strength of the Ti and Ti–5W alloy foams. We also evaluated hardness and wear resistance for our Ti and Ti–5W alloy foams. The Ti–5W alloy foam showed superior hardness and wear resistances to those of the Ti foam, which is consistent with the surface hardness result before and after the wear test. The improved hardness and wear resistance is mainly attributed to the solid-solution strengthening effects of W. This study further investigated the superior wear resistance of Ti–5W alloy foam and applied the orientation-averaging model for better predicting strength properties of the new Ti–5W alloy foam, which we believe that is considered important toward advancing biomedical implant applications of freeze-cast materials.

Acknowledgements

This research was supported by the Basic Science Research Program (NRF-2015R1D1A1A01060773) and the Priority Research Centers Program (2009-0093814). H. Choe also acknowledges support from the National Research Foundation (NRF-2014R1A2A1A11052513). Shil'ko also acknowledges support from the Belarusian Fund of Fundamental T16R-202. J. Gubicza acknowledges the financial support of the Hungarian Scientific Research Fund, OTKA, Grant no. K-109021.

Appendix A. Supplementary material

Supplementary data associated with this article can be found in the online version at <http://dx.doi.org/10.1016/j.jmbbm.2017.04.020>.

References

- Adell, R., Hansson, B.O., Brånemark, P.I., Breine, U., 1970. Intra-Osseous anchorage of dental prostheses. *Scand. J. Plast. Reconstr. Surg.* 4, 19–34.
- Choe, H., Abkowitz, S.M., Abkowitz, S., Dunand, D.C., 2005. Effect of Tungsten dissolution on the mechanical properties of Ti–W composites. *J. Alloy. Compd.* 390, 62–66.
- Choe, H., Abkowitz, S.M., Abkowitz, S., Dunand, D.C., 2008. Mechanical properties of Ti–W alloys reinforced with TiC particles. *Mater. Sci. Eng. A* 485, 703–710.
- Choi, M., Hong, E., So, J., Song, S., Kim, B.-S., Yamamoto, A., Kim, Y.-S., Cho, J., Choe, H., 2014. Tribological properties of biocompatible Ti-10W and Ti-7.5TiC-7.5W. *J. Mech. Behav. Biomed. Mater.* 30, 214–222.
- Davis, N.G., Teisen, J., Schuh, C., Dunand, D.C., 2001. Solid-state foaming of titanium by superplastic expansion of argon-filled pores. *J. Mater. Res.* 16 (5), 1508–1519.
- Dearnley, P.A., Dahm, K.L., Çimenoglu, H., 2004. The corrosion–wear behavior of thermally oxidised CP-Ti and Ti-6Al-4V. *Wear* 256, 469–479.
- Deville, S., 2010. Freeze-casting of porous biomaterials: structure, properties and opportunities. *Materials* 3 (3), 1913–1927.
- Donachie, M.J., 2004. Titanium; a technical guide, 2nd edition. ASM International, USA.
- Enderle, J., Blanchard, S., Bronzino, J., 2005. Introduction to Biomedical Engineering, 2nd edition. Elsevier academic press. ELSEVIER.
- Erk, K.A., Dunand, D.C., Shull, K.R., 2008. Titanium with controllable pore fractions by thermally reversible gel casting of TiH₂. *Acta Mater.* 56, 5147–5157.
- Fan, Z., Miodownik, A.P., Tsakirooulos, P., 1993. Microstructural characterisation of two phase materials. *Mater. Sci. Technol.* 9, 1094–1100.
- Frary, M., Abkowitz, S., Abkowitz, S.M., Dunand, D.C., 2003. Microstructure and mechanical properties of Ti/W and Ti-6Al-4V/W composites fabricated by powder-metallurgy. *Mater. Sci. Eng. A* 344, 103–112.
- Geetha, M., Singh, A.K., Asokamani, R., Gogia, A.K., 2009. Ti based biomaterials, the ultimate choice for orthopaedic implants – A review. *Prog. Mater. Sci.* 54 (397–342).
- Gibson, L.J., Ashby, M.F., 1982. The mechanics of three-dimensional cellular materials. *Proc. R. Soc. Lond. A* 382, 43–59.
- Gibson, L.J., Ashby, M.F., 1997. Cellular Solids: Structure and Properties. Cambridge University Press, New York.
- Goldade, V., Shil'ko, S., Neverov, A., 2016. Smart Materials Taxonomy. Taylor & Francis Group, Abingdon, UK.
- Gurland, J., 1958. The measurement of grain contiguity in two-phase alloys. *Trans. Metal. Soc. AIME* 212, 452–455.
- Hong, E., Ahn, B.Y., Shoji, D., Lewis, J.A., Dunand, D.C., 2011. Microstructure and mechanical properties of reticulated titanium scrolls. *Adv. Eng. Mater.* 13 (12), 1122–1127.
- Iijima, D., Yoneyama, T., Doi, H., Hamanaka, H., Kurosaki, N., 2003. Wear properties of Ti and Ti-6Al-7Nb castings for dental prostheses. *Biomaterials* 24 (8), 1519–1524.
- Jiang, P., He, X.L., Li, X.X., Yu, L.G., Wang, H.M., 2000. Wear resistance of a laser surface alloyed Ti-6Al-4V alloy. *Surf. Coat. Technol.* 130, 24–28.
- Jo, H., Kim, M., Choi, H., Sung, Y., Choe, H., Dunand, D.C., 2016. Morphological study of directionally freeze-cast nickel foams. *Metall. Mater. Trans. E* 3, 46–54.
- Jorgensen, D.J., Dunand, D.C., 2011. Structure and mechanical properties of Ti-6Al-4V with a replicated network of elongated pores. *Acta Mater.* 59, 640–650.
- Krishna, B.V., Bose, S., Bandyopadhyay, A., 2007. Low stiffness porous Ti structures for load-bearing implants. *Acta Biomater.* 3, 997–1006.
- Li, H., Oppenheimer, S.M., Stupp, S.I., Dunand, D.C., Brinson, L.C., 2004. Effect of pore morphology and bone ingrowth on mechanical properties of microporous titanium as an orthopaedic implant material. *Mater. Trans.* 45 (4), 1124–1131.
- Li, J.C., Dunand, D.C., 2011. Mechanical properties of directionally freeze-cast titanium foams. *Acta Mater.* 59, 146–158.
- Lina, H.-Y., Bowers, B., Wolan, J.T., Cai, Z., Bumgardner, J.D., 2008. Metallurgical, surface, and corrosion analysis of Ni–Cr dental casting alloys before and after porcelain firing. *Dent. Mater.* 24, 378–385.
- Liu, X., Chu, P.K., Ding, C., 2004. Surface modification of titanium, titanium alloys, and related materials for biomedical applications. *Mater. Sci. Eng. R* 47, 49–121.
- Mante, F.K., Baran, G.R., Lucas, B., 1999. Nanoindentation studies of titanium single crystals. *Biomaterials* 20, 1051–1055.
- Mondal, D.P., Das, S., Jha, Nidhi, 2009. Dry sliding wear behaviour of aluminum syntactic foam. *Mater. Des.* 30, 2563–2568.
- Moongkhamklang, P., Elzey, D.M., Wadley, H.N.G., 2008. Titanium matrix composite lattice structures. *Compos. Part A* 39, 176–187.
- Oldani, C., Dominguez, A., Fokter, S. (Eds.), 2012. Titanium as a Biomaterial for Implants, Recent Advances in Arthroplasty. InTech, Croatia.
- Park, H., Choi, M., Choe, H., Dunand, D.C., 2017. Microstructure and compressive behavior of ice-templated copper foams with directional, lamellar pores. *Mater. Sci. Eng. A* 679, 435–445.
- Queheillalt, D., Deshpande, V., Wadley, H., 2007. Truss waviness effects in cellular lattice structures. *J. Mech. Mater. Struct.* 2, 1657–1675.
- Shil'ko, S., 2011. Adaptive composite materials: bionics principles, abnormal elasticity, moving interfaces. In: Tesinova, P. (Ed.), *Advances in Composite Materials – Analysis of Natural and Man-Made Materials*. InTech Publishing Inc., Rijeka, Croatia, pp. 497–526.
- Thelen, S., Barthelat, F., Brinson, L.C., 2004. Mechanics considerations for microporous titanium as an orthopedic implant material. *J. Biomed. Mater. Res.* 69A, 601–610.
- Tuncer, N., Arslan, G., 2009. Designing compressive properties of titanium foams. *J. Mater. Sci.* 44 (6), 1477–1484.
- Venkataraman, B., Sundararajan, G., 2000. Correlation between the characteristics of the mechanically mixed layer and wear behavior of aluminum, Al-7075 alloy and Al-MMCs. *Wear* 245, 22–38.
- von Recum, A.F., 1999. Handbook of Biomaterials Evaluation; Scientific, Technical, and Clinical Testing of Implant Materials, 7th edition. Taylor & Francis, USA.
- Wang, Y.B., Li, H.F., Cheng, Y., Zheng, T.F., Ruan, L.Q., 2013. In vitro and in vivo studies on Ti-based bulk metallic glass as potential dental implant material. *Mater. Sci. Eng. C* 33, 3489–3497.